One-dimensional patterns and topological defects in smectic liquid crystal films

Bruno Zappone, Emmanuelle Lacaze

One-dimensional patterns and topological defects in smectic liquid crystal films

Bruno Zappone[1] *and Emmanuelle Lacaze*[2]

[1] Consiglio Nazionale delle Ricerche – Istituto di Nanotecnologia (CNR-Nanotec), Via P. Bucci, 33/C, Rende (CS) – 87036 Italy

[2] Sorbonne Université, Faculté des Sciences, CNRS, Institut des Nanosciences de Paris (INSP), 4 place Jussieu 75005 Paris, France

ABSTRACT. Smectic liquid crystals exhibit a remarkable ability to self-organize into a variety of textures, patterns, and arrays extending over large surface areas with microscale periodicity. These structures provide a useful platform for the bottom-up fabrication of microdevices and functional materials, such as microlens arrays and nanoparticle templates. Periodic structures appear in response to a conflict of director alignment created within the smectic film by external fields such as hybrid (planar-homeotropic) anchoring conditions at the film interfaces or an electric field applied normal to the surface anchoring direction. In this article, we review the formation, structure, and applications of one-dimensional (1d) patterns obtained in response to a director bend, typically induced by unidirectional hybrid anchoring conditions in thin films or under applied electric fields. Compared to lattices of focal conic, 1d patterns harbor an unusual array of topological defects, including disclination and dislocation lines, grain boundaries, and curvature walls, running along periodically spaced and bend-free cylindrical stacks of smectic layers. These defects, most of which have been described by Maurice Kleman, appear to drive the structural evolution of 1d patterns as a function of the film thickness. Under unidirectional hybrid anchoring, the defects are oriented perpendicular to the planar anchoring direction and provide highly anisotropic templates for building ordered networks of close-packed nanoparticles. Moreover, the array formation at the transition from the nematic to the smectic phase is intimately connected to the smectic phase frustration by bend distortions, producing an "intermediate" smectic with partial penetration of the bend distortion through undercooled nematic domains

1. Introduction

A hundred years ago, Georges Friedel recognized the lamellar structure of the smectic (*S*) phase by observing periodic defect patterns in liquid crystal (LC) films [1]. Since then, scientists have been fascinated by the diversity and complexity of self-ordered patterns, textures, and arrays appearing in various LC phases. These structures typically emerge to settle a conflict of molecular alignment created in the LC film by surface anchoring interactions [2-4] and applied fields [5, 6]. Because LC patterns exhibit a microscale period decreasing with the film thickness, they provide a rapid and inexpensive "bottom-up" alternative to "top-down" microfabrication methods such as ion beam and photolithography, with the advantage of fast and large response to external stimuli. For example, patterns eventually disappear as the temperature increases (e.g., at the transition to the isotropic phase) and their morphology can be tuned by applying an electric field [7-9]. Moreover, LC micropatterns are optically anisotropic and have been used as optical gratings [10] and microlens arrays to focus light [11, 12] and generate optical vortices [13].

In the *S* phase, the LC molecules tend to align with each other side-by-side, creating a one-dimensional (1d) density modulation with nanoscale period a_0 (Fig. 1a) [14]. Many properties of the *S* phase can be understood in analogy with a layered material having a layer thickness a_0, assuming a fixed angle between the layers and the molecular director **n**. The angle is zero or non-zero in the smectic-*A* (S_A) and smectic-*C* (S_C) phases, respectively. Large elastic bending of the layers can be obtained under conflicting aligning fields as long as the layer thickness a_0 is preserved [15]. This folding of the layers creates confocal stacks with shared centers of curvature, such as concentric spheres and cylinders [16, 17], and focal conic domains (FCDs, Fig. 1) [18]. The centers of curvature of a confocal stack are the cores of topological defects of the director field.

Figure 1 – see end of the document

In a S_A curved confocal stack, there is at least one plane such that **n** makes a constant angle with the plane (Fig. 1). For example, in any plane containing the central disclination of a cylindrical stack, **n** is normal to the disclination and parallel to the plane (Fig. 1c). In a plane containing the ellipse or hyperbola of a FCD, **n** lies in the plane with a variable in-plane orientation (Fig. 1d). In a curved confocal stack, however, **n** cannot have constant angles on two parallel planes (Fig. 1b-c). Therefore, a curved confocal stack confined in a flat film (with

non-deformable interfaces) can satisfy the anchoring condition on one interface at most, possibly with a preferred in-plane direction (easy axis), but it cannot fill the film without breaking at least one of the anchoring conditions. For this reason, the smectic film can only comprise the domain of a stack that most closely matches the boundary conditions. These matching domains appear over the entire surface area and self-assemble into close-packed periodic patterns (Figs 2 and 3), creating topological defects at the domain boundaries. The lateral size of the confocal domains and the pattern period typically are of the order of the film thickness, whereas the defect cores typically have nanoscale dimensions. Because the cores match the size of nanoparticles, defect arrays in smectic LC patterns have been used to guide nanoparticle assembly into functional shapes over large film areas [19-27]. The energy cost of anchoring breaking disappears at a deformable interface when the interface is curved confocally. The curvature, however, also increases the area and surface energy. As a consequence the shape of the deformable interface does not correspond to any layer of the confocal stacks. Indeed, atomic force microscopy (AFM) measurements show topographical features at the interface that are much shallower and less curved than those expected at the free surface of a confocal stack (Fig.2b, Fig.3d). The Topographic micropatterns characterized by surface undulations have found a promising application as templates for soft lithography [21, 28, 29].

A common type of defect pattern observed in the S_A phase is the two-dimensional (2d) "honeycomb" lattice comprising axisymmetric toroidal FCD such that the ellipse and hyperbola degenerate into a circle and a line defect, respectively (Fig. 2). This pattern type is usually obtained in open films with degenerate "hybrid" surface alignment conditions, e.g., normal anchoring at the air interface and planar degenerate anchoring at the interface with an isotropic material [19, 21, 30, 31]. In this case, the circle of the toroidal FCD lies on the surface that imposes planar anchoring. Honeycomb-like lattices of non-toroidal FCDs (Fig. 1d) can be obtained when the degeneracy of the planar alignment is lifted, e.g., on anisotropic substrates such as rubbed polymers [32-36] and mica [37]; in the presence of gradients of film thickness [38]; and when the S_A phase develops from the non-uniform director field surrounding a defect of the *N* phase [31]. These non-toroidal FCDs, however, significantly differ from toroidal FCD in their internal structure [37] and response to changes in film thickness *h*. Notably, the 2d patterns appear under unidirectional anchoring conditions only if *h* is sufficiently large, whereas 1d patterns are observed in thin films.

Figure 2 – see end of the document

One-dimensional patterns were introduced by Parodi [9], who analyzed the electro-optical effect theoretically in a uniform homeotropic S_A film with normal anchoring conditions at both surfaces. Parodi predicted that a magnetic field parallel to the surface would create a periodic 1d array of confocal hemicylinders (i.e., one half of the cylindrical roll in Fig 1c) with their axes perpendicular to the field. He tentatively proposed various models for filling the space between the hemicylinders, including an iterative Apollonius packing with rolls of decreasing diameter, grain boundaries, dislocations, and melting of the layered phase. Similar 1d patterns were obtained experimentally a few years later by Goscianki *et al* [7]. By applying sufficiently strong electric fields in the direction normal to a uniform S_A film with planar anchoring conditions, they obtained stripes perpendicular to the planar anchoring direction. In 1978, Allet, Kléman, and Vidal [39] obtained analogous 1d stripe patterns without applying any field in S_C films deposited in air on anisotropic silicon oxide substrates that induced unidirectional planar anchoring. They proposed a model based on an array of confocal hemicylinder (one half of the cylindrical roll in Fig 1c) in contact with the solid substrate, as proposed by Parodi [9], covered by an almost horizontal stack of slightly undulated layers at the air interface. They also argued that a vertical curvature wall, i.e., a grain boundary perpendicular to the planar anchoring, should be expected between two confocal hemicylinder domains. These studies, however, were conducted mainly by observing the smectic films between crossed polarizers. Therefore, the layer arrangement inside the LC film was not experimentally determined and theoretical models could not be validated.

In 2004, the interest in 1d patterns was revived by a study by Michel *et al* [40] on S_A films deposited in air on molybdenite (Fig. 3a). Not only did the films show 1d patterns perpendicular to the planar anchoring direction in the absence of any field, but this observation was followed by a series of synchrotron x-ray scattering measurements. Their findings revealed a complex defect network and suggested the presence of a strongly distorted undercooled *N* phase in very thin films [40-42]. More recently, 1d patterns containing linear and ribbon-like defects have been studied as a promising platform to guide the assembly of nanoparticles into "nanochains" [20, 22, 24] or oriented 2d networks [20], and to align anisotropic particles [26, 27, 43] over large surface areas. The 1d patterns have also been recently obtained under different alignment geometries, notably by applying electric fields [8] and through accurate photo-patterning of polymer substrates [44]. In the absence of applied

fields, 1d patterns are caused by the conflict of alignment imposed by the surfaces, i.e., incompatible homeotropic and unidirectional planar anchoring conditions. A comparison with toroidal FCDs obtained under degenerate hybrid anchoring conditions (Fig. 2) suggests that the circle defects at the planar anchoring surface evolve in the 1d patterns into straight disclination lines, forming the center defects of quarter cylinders, perpendicular to the planar anchoring direction *x* (Fig. 3e). The straight vertical line, on the other hand, expands into a curvature wall in the vertical *yz* plane (Fig. 3e) of much higher energy (per unit length along the *x*-axis) than the line defects of toroidal FCDs. There is an intimate connection between phase frustration and nucleation of various defect topologies [1, 8, 19, 33, 37, 40, 41, 45-51], which is an intriguing aspect of pattern formation in smectic LC films and has provided a fertile ground for testing Kleman's theory [52]. In this article, we review the experimental evidence of defect formation in smectic S_A films that are deformed in the vertical *xz*-plane perpendicular to the film plane, but are invariant along the *y*-axis (Fig. 3e). Namely, we consider films with unidirectional hybrid anchoring conditions imposed along the *x*- and *z*-axis, and electric fields applied either along the *z*-axis or the *y*-axis.

In the first part, we describe a hemicylindrical stacking revealed by synchrotron x-ray diffraction, polarized optical microscopy (POM), and atomic force microscopy (AFM) within the 1d patterns. Then, we discuss the analogy between the Landau-de Gennes energy of a S_A material with bent director and that of a type-I superconducting metal in a magnetic field. The bend distortion frustrates and 'melts' the S_A phase into periodically spaced domains of undercooled nematic phase (*N*), in the same way as the magnetic field depresses the transition from the normal metal to the superconducting state. The discussion is followed by an experimental survey of thin smectic films, where x-ray scattering measurements have elucidated a defect network structure within 1d patterns. We then discuss the structural evolution of these distorted smectic films as a function of the film thickness *h*, which appears to be specifically driven by the necessity to avoid defects. We also show that a transition between 2d FCD lattices and 1d patterns can be equally produced by reducing the film thickness *h* or applying an electric field. Finally, we describe the application of these structures for the templating of nanoparticle assemblies, where topological defects are able to confine, organize, and align nanoparticles of various shapes. Recent results on the control of localization, orientation, and large-scale patterning of the 1d patterns are also presented.

2. Pattern formation under unidirectional hybrid anchoring conditions

2.1. Flattened hemicylinder domains

Grazing incidence x-ray scattering (GISAXS) has been used to study 4-n-octyl-4'-cyanobiphenyl (8CB) films of thickness varying between $h \approx 450$ nm deposited on molybdenite substrates in air (Fig. 3a-b), for which 1d pattern formation was observed by combining POM (Fig. 3c) and AFM (Fig. 3d) [40]. For a magnitude $q_0 = 2$ nm^{-1} of the wave-vector transfer **q**, corresponding to the 8CB layer thickness $a_0 = 2\pi/ q_0 = 3.16$ nm, the scattered intensity is proportional to the number of smectic layers perpendicular to **q**. When **q** was parallel to the substrate and the sample was rotated around the substrate normal, the scattered intensity was different from zero only when **q** was normal to the planar anchoring direction *x* (Fig. 3a). On the other hand, when **q** was continuously tilted from an orientation almost parallel to the substrate (tilt angle $\alpha = 7°$) to an orientation almost perpendicular to the substrate ($\alpha = 80°$), the scattered intensity was almost constant but with a slight increase (3b). This result is consistent with layers folded confocally into quarter cylinders having their center at the planar anchoring surface and parallel to the *y*-axis (Fig. 3e). According to Parodi [9] and Allet *et al* [39], the quarter cylinders should be directly joined into a hemicylinder with height *h* and width 2*h*, forming a 1d pattern with period $d = 2h$. Instead, POM (Fig. 3c) and AFM (Fig. 3d) images showed that *d* is systematically larger, suggesting that the quarter cylinders are found at the edges of "flattened" hemicylinder with $d > 2h$ (Fig. 3e). The presence of a large number of horizontal layers in the center of the flattened hemicylinders is demonstrated by an increase of scattered intensity from $\alpha = 80°$ to a maximum at $\alpha = 90°$ (Fig. 3b–Inset). Indeed, a 90° orientation of **q** corresponds to horizontal smectic layers parallel to the substrate. Moreover, AFM images of the 1d patterns showed a shallow depression at the boundary between two hemicylinders, with depth much smaller than *h* (Fig. 3d). This observation shows that the space at the boundary between two hemicylinders was filled with a vertical curvature wall in the *xy*-plane (Fig. 3e). This also agrees with the slight increase of intensity shown in Fig. 3b when α increases. Therefore, these findings reveal an internal structure of the 1d patterns more complex than a simple array of hemicylinders.

Figure 3 – see end of the document

These 1d stripe patterns, also known as "oily streaks", have been observed for a wide variety of smectic LCs, including 8CB and other alkyl-cyanobiphenyls [53], alyloxy-cyanobyphenyls

(8OCB) [35], SCE12 [8], 4-n-pentylphenylthiol-40-noctyloxybenzoate (8S5), and 9004 [50]. The patterns have been obtained by depositing thin LC films in air (imposing homeotropic anchoring) on various substrates that impose unidirectional planar anchoring, such as molybdenite [40], mica [47, 48], rubbed polyvinylalcohol (PVA) [49], rubbed polyimide (PI) [50], and the photoalignment agent sulfonic azo dye SD1 [44]. It has also been shown to occur in cells where homeotropic anchoring was imposed by layers of octadecyl-trimethoxy-silane (OTS), while planar anchoring was imposed by rubbed PVA or PI [8]. The nature of the substrate and possibly the use of a cell instead of an open film appears to play a significant role in determining the internal array structure. Indeed, the array period d increased as a function of the film thickness h with a variable slope in different samples: $\partial d/\mathrm{d}h = 1.5$ in open films on PVA [49], $\partial d/\mathrm{d}h = 2$ in open films on sulfonic azo dye SD1 [44] and in closed cells [8], and $\partial d/\mathrm{d}h = 4.4$ in open films on molybdenite [40]. The film thickness h appears to be the most important critical parameter for the appearance of 1d patterns. This is illustrated by the fact that 1d patterns appear at small h and eventually transform into a 2d FCD lattice when h increases [35, 37, 44, 47]. The transition typically occurs for h of the order of a few micrometers, although the exact value for the critical thickness varies with the substrate type [37] [44].

Unidirectional hybrid anchoring conditions tend to introduce both bend and splay distortions in the director field. As the film thickness h decreases and the elastic energy increases, a possible way to release the director strain is to break the anchoring and let the pattern structure yield at some critical thickness depending on the anchoring strength. Yet, 1d patterns can be observed in films as thin as 60 nm [42], indicating that anchoring breakage does not occur as the energy increases.

2.2. Smectic phase frustration by bend director distortions

Despite its simple geometry, the smectic phase is one of the most enigmatic objects in statistical physics. Modeling the phase behavior in complex geometries, particularly near the transition with the N phase, is a major theoretical and computational challenge [51, 54, 55]. The smectic order can be represented with a complex order parameter $\rho = \psi e^{i\varphi}$ such that $|\psi|$ is the magnitude of the molecular density modulation and the phase φ is a multiple of 2π on a set of surfaces. The phase gradient $\nabla\varphi$ is normal to these surfaces, and the distance between

two consecutive surfaces or "layer thickness" is $a_0 = 2\pi/|\nabla\varphi|$. In the non-deformed ground state, ψ is uniform on parallel planes that are equally spaced by $a_0 = 2\pi/q_0$. In the S_A phase, the director **n** tends to be normal to the surfaces, so that $\nabla\rho = i\rho\nabla\varphi = iq_0\rho\mathbf{n}$ in the ground state. Therefore, the free energy density of a distorted state is expected to increase quadratically as a function of the strain field $\nabla\rho - iq_0\rho\mathbf{n}$. Because this field couples ρ and **n**, director distortions can affect the smectic order and vice-versa. In 1972, de Gennes proposed the following Landau-Ginzburg expansion for the free energy density near the N-S_A phase transition [15]:

$$f = f_S(\psi,T) + f_N(\mathbf{n}) + (c_{||}/2)\left|(\nabla_{||} - iq_0\mathbf{n})\rho\right|^2 + (c_\perp/2)\left|\nabla_\perp\rho\right|^2 \qquad (1)$$

where $||$ and $\perp$ indicate the direction of **n** and the perpendicular plane, respectively. The first term in Eq. (1), f_S, is the energy required to create an undistorted smectic with amplitude ψ of the smectic order at temperature T. This term becomes negative at the transition temperature T_0. The second term, f_N, is the Frank-Oseen elastic energy of the director field **n**, with three terms proportional to $(\nabla\cdot\mathbf{n})^2$, $[\mathbf{n}\cdot(\nabla\times\mathbf{n})]^2$, and $|\mathbf{n}\times(\nabla\times\mathbf{n})|^2$ corresponding to splay, twist, and bend distortions, respectively. The last two terms describe the coupling between the smectic order and director field due to the strain. The coupling disappears when $\nabla\rho = iq_0\rho\mathbf{n}$, in which case ψ is the same uniform field as in the ground state and $\nabla\varphi = q_0\mathbf{n}$, i.e., the director is normal to equally spaced (confocal) layers. Because $\nabla\times\nabla\rho = 0$, a necessary condition to avoid coupling is that the director field be irrotational, i.e., $\nabla\times\mathbf{n} = \mathbf{0}$. This implies that both twist and bend distortions must be removed to nucleate the smectic phase in a distorted nematic. On the other hand, splay distortions with $\nabla\cdot\mathbf{n} \neq 0$ increase the elastic energy of the director field without affecting the smectic order.

De Gennes pointed out that Eq. (1) is analogous to the free energy expansion of metals near the transition to the low-temperature superconducting state [15]. In this case, the complex field ρ is the wavefunction of Cooper electron pairs, **n** is the vector potential, and $\mathbf{B} = \nabla\times\mathbf{n}$ is the magnetic field. In a phase diagram where T and $B = |\mathbf{B}|$ are taken as the x- and y-axis, respectively, there is a critical line with points (T_c, B_c) for the metal-superconductor transition, and the line has a negative slope, i.e., $\partial T_c/\partial B_c < 0$ (Fig. 4a).

At the transition to the superconducting state, **B** tends to be expelled from the bulk (Meissner effect). Immediately below the critical line, however, the expulsion is incomplete and

inhomogeneous, and **B** penetrates the superconductor. In a type-I superconductor film, finite-sized domains of undercooled normal metal state, carrying the **B** field, become intermixed with superconductive domains in a pattern of meandering stripes or polygonal meshes known as an intermediate state [56-58] (Fig. 4a). In type-II superconductors, **B** penetrates via a 2d array of elementary defects (vortices) known as Abrikosov lattice [56].

The analogy with superconductors helps in predicting the behavior of LC films near the N-S_A phase transition under strong director distortions. The N and S_A phases are analogous to the normal and superconducting states of metals, and the director rotor $\nabla\times\mathbf{n}$ (i.e., twist and bend distortions) tends to be expelled at the transition from the N phase to the S_A phase [15]. In type-II thermotropic LCs, de Gennes' analogy led to the discovery of twist grain boundary (TGB) phases in chiral thermotropic LCs, where the twist field penetrates as a set of periodically spaced screw dislocations analogous to the Abrikosov vortex lattice [59, 60]. Twist-induced type-I behavior has been observed at the transition between the cholesteric (N^*) and S_A phases in cyanobiphenyls and cholesteryl esters [61-63]. On the other hand, bend-induced type-I behavior has been reported only a few times in the history of LCs [64, 65]. This is surprising because the molecular structure of thermotropic LCs used in common applications suggests a type-I behavior [14, 59] and a simple test of the critical properties was suggested already by de Gennes using hybrid anchoring conditions [15].

Figure 4 – see end of the document

The connection between 1d pattern formation in S_A films with unidirectional hybrid anchoring and the transition from the N phase into an "intermediate" LC phase [35] has been explored only recentlyexplored. The anchoring conditions produced a splay-bend distortion with amplitude $B = |\nabla\times\mathbf{n}| \approx 1/h$ in the N phase, where h is the film thickness [15]. Therefore, the transition to the S_A phase can be studied in a (T, B) phase diagram where the critical line is expected to have a negative slope (Fig. 4a). As T was decreased below the phase transition temperature T_0, a 2d FCD lattice formed for large h (i.e., small B), whereas a 1d pattern perpendicular to the planar anchoring direction was obtained for small h (i.e., large B) (Fig. 4b). The 2d pattern corresponds to the S_A phase with complete director curl expulsion, because the FCD is a confocal layer stacking compatible with the S_A phase structure. It maps into the lower-left corner of the (T, B) phase diagram (Fig. 4a). The 1d pattern, on the other hand, can be associated with an intermediate state at points (T, B) just below the critical line.

In this state, the bend distortion is expelled from the S_A phase into domains of undercooled *N* phase. The observation that 1d patterns expand from thick to thin regions of the film as *T* decreases shows that the critical temperature T_c of the transition from the *N* phase to the intermediate phase decreases when *B* increases, i.e., the critical line has the expected negative slope, $\partial B_c/\partial T_c < 0$ (Fig. 4a). Moreover, T_c depends on the film thickness *h* according to a power law, $T_c/T_0 = 1 - (h_0/h)^{\gamma}$ with a critical exponent γ close to unity and characteristic length $h_0 = 0.6$ nm, in agreement with calculated values [35]. For a given thickness *h*, the period of the 1d patterns increases when the temperature is decreased [35], indicating that the undercooled *N* domains evolve as a function of the temperature.

2.3. Topological defects in thin films

For smectic films with sufficiently small thickness *h* and unidirectional hybrid anchoring conditions, 1d patterns are observed well below T_0, down to room temperature. To determine the type of defects and the possible presence of *N* domains, thin 8CB films with different thicknesses *h* have been studied on molybdenite using GISAXS [41] and on rubbed PVA using a combination of GISAXS, transmission small-angle x-ray Scattering (TSAXS), and ellipsometry [49]. On molybdenite, the scattered x-ray intensity showed a number of layers almost constant as a function of the tilt angle α (angle between the layer normal and the substrate – the wave-vector transfer **q** orientation) for films with thickness $h \approx 450$ nm (Figs 3b and 5a), consistent with a structure mainly made of layers folded confocally into quarter cylinders [40]. When the thickness decreased to $h = 150$ nm, however, the number of layers measured at $\alpha = 20°$ became around six times larger than the number measured at $\alpha = 60°$ (Fig. 5a) [41]. Similar results hold for 8CB on rubbed PVA substrates [49], i.e., the intensity variation with α is maximum for the smallest thickness (Fig. 5a) [41]. The topology of the director field and smectic layer structure close to the substrate is not expected to vary as *h* decreases, i.e., when the LC is removed from the top of the film. In other words, defects near the surface are the same in thin films and thick films as long as a 1d pattern is formed. Therefore, x-ray scattering measurements become increasingly sensitive to these defects as *h* decreases. The decreasing number of layers observed when α increases can be explained by introducing a rotating grain boundary that joins horizontal smectic layers from the center of the flattened hemicylinders with curved layers at the hemicylinder edge (i.e., in the quarter

cylinders) (Fig. 5b) [41, 49]. Such rotating grain boundary replaces the dislination line on the substrate and the curved layers close to the quarter cylinder center, where the elastic energy diverges. X-ray data allow for the extraction of the rotating grain boundary profile showing that dislocations are absent from the rotating grain boundary close to the substrate [49], whereas they populate the upper part approximately 50 nm above the substrate (Fig. 5b). The structure of the vertical curvature wall at the boundary between two flattened hemicylinders is still unclear. The director is discontinuous across the wall and the bend distortion is large near the substrate. Although dislocations are expected near the substrate, a disclination with topological charge $s = -1/2$ has also been suggested near the air interface [35, 50, 51]. It is delicate to confirm these features via x-ray analysis, as they are associated with values of tilt angle α that are too small or too large. Moreover, on PVA, a combination of TSAXS and ellipsometry measurements revealed a horizontal grain boundary at the center of the flattened hemicylinders (in green in Fig. 5b), joining flat horizontal layers originating from the air interface (homeotropic director orientation) with flat vertical layers originating from the substrate (planar orientation) [49]. The length of this horizontal grain boundary along the *x*-axis is around 400 nm. Most likely, undercooled *N* domains form close to the transition temperature T_0 in the regions where the dislocations and horizontal grain boundary have been detected by x-ray experiments at room temperature. As the temperature is decreased from T_0, the size of the *N* domain decreases to reach the nanoscale dimension of smectic defect cores at room temperature. Finally, 1d patterns in thin smectic films with unidirectional hybrid anchorings can be viewed as periodic networks of 1d and 2d topological defects, i.e., dislocations and central grain boundaries, respectively, the dislocations being localized at the upper part of the rotating grain boundary and possibly at the basis of the vertical curvature wall.

Figure 5 – see end of the document

Topological defects in thin smectic films could *a priori* depend on the strength of surface anchoring, which varies as a function of substrate chemistry, e.g., between PVA and molybdenite, and physical properties, e.g., different surface morphology obtained on PVA using different rubbing protocols. Relating defect formation to anchoring energy, however, is particularly challenging in the S_A phase compared to the *N* phase [66]. The comparison between PVA and molybdenite provides some insights. The slope of the period vs. thickness curve measured for one S_A material (8CB) varies from 4.4 on molybdenite to 1.5 on PVA. The

similarity between x-ray data obtained on molybdenite and on PVA [41, 49] indicates that the rotating grain boundary does not vary with the substrate, as it reflects the necessity to remove the highly curved layer around quarter cylinder centers. The substrate dependence might thus not concern so much the rotating grain boundary and dislocations lines as the horizontal central grain boundary (in green in Fig. 5b). Its presence has been demonstrated on rubbed PVA, where the substrate is entirely covered by perpendicular layers. This may be due to the large anchoring energy on PVA [67]. For a thickness $h \approx 150$ nm, the larger slope $\partial d/\partial h = 4.4$ on molybdenite demonstrates that the width of the flattened hemicylinders on molybdenite (along the anchoring direction x, Fig. 3e) is significantly larger than on PVA, respectively 1.1 µm and 600 nm. On molybdenite, the horizontal grain boundary in the center of the flattened hemicylinders most likely is replaced by flat horizontal smectic layers that directly reach the molybdenite substrate and break the planar anchoring. The planar anchoring could be broken at a low cost on molybdenite, thereby creating large flattened hemicylinders (i.e., more extended in the x-direction), whereas anchoring is so strong on PVA that a horizontal grain boundary must be created instead of breaking the anchoring, implying a much higher energy per unit length (along x) and therefore a shorter extension of the flattened hemicylinders. This evolution from molybdenite to rubbed PVA underlines how the nature of the substrate in relation with the anchoring enrgy values may at least partly drive the nature of the topological defects formed within the 1d patterns associated with unidirectional hybrid anchoring conditions.

2.4. Pattern evolution with the film thickness

2.4.1. One-dimensional patterns (intermediate thickness)

The pattern evolution as a function of the film thickness h has been studied by combining POM and GISAXS for 8CB droplets that spread into thin films on cleaved sheets of muscovite mica [4]. For $h \approx 1$ µm, the evolution of scattered x-ray intensity as a function of smectic layers orientation was very different from the one observed for thin films (Fig. 6a). The intensity increased when α increased (Fig. 5a), showing that the number of smectic layers increased from $\alpha = 20°$ to $\alpha = 90°$, in contrast with thin films deposited on rubbed PVA [49] and molybdenite [41]. These findings were explained considering that the layers were folded confocally around a virtual disclination located around 100 nm below the substrate (Fig. 6b).

The expulsion of the disclinations from the bulk allows forming the rotating grain boundaries (in red in Fig. 6b) that connect the layers to layers perpendicular to the substrate without any dislocation along the grain boundaries. A minimum thickness of a few hundred nanometers is geometrically required for such a structure (Fig. 6b). Therefore, films thinner than this minimum thickness can transform into a structure similar to the one found on rubbed PVA and on MoS_2. Such transformation has indeed been evidenced for the thinnest 8CB films on mica [4].

Figure 6 – see end of the document

The results on mica indicate that, in the presence of a sufficiently small bend in thick films, topological line defects can be avoided and remain virtual. Again disclinations are expulsed but without introducing rotating grain boundaries or dislocations. Moreover, horizontal grain boundaries are also avoided. A critical bend value corresponding to a sufficiently small thickness is necessary to impose the formation of this large number of topological defects. A critical bend value defining two different 1d patterns has yet been observed for mica substrate only. However, a critical bend between 1d and 2d patterns has been observed for most substrates.

2.4.2. Two-dimensional patterns (large thickness)

Figure 7 – see end of the document

When mica is used as a substrate and the thickness is further increased by a few micrometers, the structure changes from the 1d pattern to a 2d pattern of non-toroidal FCDs. This 2d pattern is found on many substrates in open films, including molybdenite and mica crystals [47], PVA and PI polymers [37], photo-aligning sulphonic azo-dye SD1 [68], and in closed cells [8, 65]. These observations agree with the general argument outlined above that a large bend distortion, i.e., small thickness and strong unidirectional hybrid anchoring conditions, are required to significantly frustrate the smectic phase and create the intermediate phase, which eventually evolves into the 1d pattern at room temperature (Fig. 4a). For larger thicknesses, even if almost hexagonal FCD lattices are formed, a close look reveals that their internal structure is very different from toroidal FCD lattices (Fig. 2). POM, polarizing fluorescence confocal microscopy (PFCM, Fig. 7a), and AFM (Fig. 7b) on open 8CB films on

mica and rubbed PI showed that the FCD is of the "square" type (Fig. 7c): the ellipse is oriented at 45° with the interfaces, whereas the conjugated hyperbola is both parallel to the planar anchoring substrate and normal to the air interface, respectively [37, 68]. Only a thin slab of the FCD structure is formed in the 8CB film so that the ellipse and hyperbola intersect the substrate (at points M and F, respectively, in Fig. 7c). These highly eccentric FCDs are close-packed into a quasi-hexagonal lattice. Anchoring conditions are violated in each lattice unit. In contrast with toroidal FCD lattices, the ellipse and hyperbola are largely virtual and layers are interrupted by the interfaces. Moreover, close-packing of non-toroidal FCDs requires creating additional defects other than the ellipse and hyperbola at the boundary between two FCDs. In contrast, the close-packing of toroidal FCDs, possibly with Apollonius tiling, does not require additional defects. Due to the fact that in 2d patterns the defects are only localized sections of 1d or 2d defects, overall they might be of lower energy than the defects of 1d patterns that are invariant along *y*-axis. This concerns especially the curvature wall that becomes of specifically large energy for large thickness. The next step would however be to calculate or at least estimate the various energies at play in these highly distorted smectic films and how they vary when the thickness increases. This would be a challenging task but would allow a more precisel understanding of how such frustrated 2d patterns can be preferred at large thicknesses.

2.5 Field-induced patterns

Positional order deeply affects the response of the S_A phase to applied stimuli, mainly because the lamellar structure is rigid to twist and bend distortions involving the director curl, $\nabla\times\mathbf{n}$. Notably, applying an electric or magnetic field to a film with uniform director $\mathbf{n}_0$ does not produce the Fréedericksz transition observed in the *N* phase. Rapini [69] showed that a similar transition could be envisioned in the S_A phase, but the field must be increased by orders of magnitude above the Fréedericksz threshold to produce a significant director reorientation at any distance from the surfaces. Increasing the applied field, however, also raises the free energy to a point where other director topologies may become thermodynamically favorable. In contrast with the Fréedericks transition and other field-induced continuous deformation (e.g., in a nematic with hybrid anchoring [36]), a discontinuous change of topology implies the nucleation or annihilation of defects and typically involves an energy barrier much larger than k_BT, where k_B is the Boltzmann factor. As a result, topological transitions induced by

applied fields typically are non-reversible so that the new director topology does not relax back to the uniform alignment when the applied field is switched off [70].

Evidence that electric and magnetic fields can create defect patterns in the S_A phase emerged in the early 1970s. Cladis and Torza [32] studied the transition from a uniform homeotropic director alignment $\mathbf{n}_0$ towards a planar alignment in films of *n-p*-cyanobenzylidene-*p*-octyloxyaniline (CBOOA) by applying a magnetic field **H** parallel to the interfaces. A 2d texture formed upon cooling into the S_A phase, similar to the FCD textures observed under hybrid anchoring conditions in the absence of fields (Figs 2b and 6). This texture did not relax back to $\mathbf{n}_0$ alignment when the field was switched off, in agreement with Rapini's results. Because two distinct states could be obtained for $H = 0$ (uniform homeotropic and 2d texture), the response was bistable. The transition from homeotropic to planar orientation under an applied electric or magnetic field proceeds through FCD nucleation, growth, and packing as well as layer undulation, and has been analyzed by Kléman and others in refs. [71-73].

Cladis and Torza [32] noted that this sequence of textures was the same observed upon cooling the LC film from the *N* phase into the S_A phase under hybrid anchoring conditions in the absence of fields (Fig. 4). This similarity reveals that the 2d texture is caused by the splay-bend director distortion in the *N* phase, which can be induced in different ways: competition between anchoring and magnetic field or unidirectional hybrid anchoring conditions. Hinov [74] found similar 2d textures by applying an electric field perpendicular to planar CBOOA films in the *N* phase and cooling in the S_A phase. This work confirmed earlier findings obtained by Goscianski *et al* [7] for the splay transition in CBOOA, 8CB, and 4-cyano-4'-*n*-octyloxybyphenyl (8OCB).

Applying a normal electric field to a homeotropic film of 4-n-butyloxy-benzylidene-4'-n-octylaniline (4O.8), a material with negative dielectric anisotropy $\varepsilon_a < 0$, Hinov *et al* [75] revealed new types of 1d patterns with 1d stripes perpendicular to the splay-bend plane. This pattern is analogous to the periodic arrangement of hemicylinder predicted by Parodi [9] and observed in thin films with unidirectional hybrid anchoring conditions (Fig. 3e). Because the anchoring conditions and electric field did not impose any orientation in the film plane, however, the orientation of FCD and stripe patterns in 4O.8 films were not fixed and created meandering patterns.

Another type of bistable response was observed by applying sufficiently strong electric fields while keeping the LC in the S_A phase. In this case, Hareng *et al* [76], Goscianski *et al* [7], Jakli and Saupe [77], and Findon *et al* [78] reported the formation of 1d patterns, whereas a 2d texture is created upon cooling from the *N* phase [7] (Fig. 8a).

Figure 8 – see end of the document

Under unidirectional planar-homeotropic hybrid anchoring conditions, Gryn *et al* [26] noted that applying an electric field *E* perpendicular to the cell in the nematic phase and decreasing temperature towards the smectic phase confines the splay-bend distortion to a thinner surface layer with a thickness comparable to the electric coherence length $\xi_E = V_c/\pi E$. Here, $V_c = \pi(K_1/\varepsilon_a)^{1/2}$ is the Fréedericksz threshold for the splay transition, K_1 is the splay elastic constant, and ε_a is the dielectric anisotropy. Therefore, increasing the field strength *E* has an effect analogous to decreasing the thickness *h* in the absence of field. Indeed, the authors showed that cooling an 8CB film from the *N* phase to room temperature produces the 2d texture in the S_A phase when *E* is smaller than a critical field E_s = (1.6 – 2.0) V/μm, whereas a 1d stripe pattern was obtained for stronger fields (Fig. 8b). Moreover, the array period *d* decreased as *E* was increased, in agreement with the decrease of *d* when *h* decreases, observed in the absence of field. This is consistent with a reduction of the confinement thickness ξ_E and an increase of bend distortion in response to an increasing electric field. The two pattern types (1d and 2d patterns) are created in response to different levels of bend distortion. Namely, the 2d texture corresponds to low bend amplitude in the *N* phase that is removed in the S_A by creating FCDs. The 1d texture, on the other hand, is analogous to the stripe textures observed in thin films with unidirectional hybrid anchoring conditions in the absence of fields, i.e., periodic arrays of confocal flattened hemicylinders separated by boundary wall and containing dislocations (see Section 2.2) [35]. The slope $\partial d/\partial \xi_E$, however, was more than twice larger than the slope $\partial d/\partial h$ observed in the absence of fields. Most likely, slightly different structures and defects are created within the 1d pattern depending on whether a field is applied [8].

We point out that field-induced patterns in hybrid 8CB films show a bistable response with a robust persistence against field variations, similarly to homeotropic smectic films under magnetic or electric fields mentioned above [8, 65]. One-dimensional patterns with period *d* created by cooling from the *N* with a sufficiently strong field persisted in the S_A when the field was reduced, increased, or switched off, with the same period *d*. Again, the bistable

behavior is due to the high energy required to nucleate and annihilate topological defects within the array. An interesting approach to avoid the bistability of 2d FCD patterns and tune their optical properties as a function of an applied field been recently been proposed by Boniello *et al* [79]. The pattern was stabilized in a 8CB film by polymerization in the S_A-phase and persisted after heating in the *N*-phase. Fast and reversible control of light transmission and diffraction was obtained by varying the amplitude of an applied electric field.

3. Applications

3.1. Nanoparticle templating

In thin 8CB films deposited on PVA in air under unidirectional planar-homeotropic hybrid anchoring conditions, topological defects can be revealed by their interaction with inorganic nanoparticles. These are known to be attracted and trapped by defect cores [80], thereby releasing the core energy and stabilizing the defect [81-86]. In this context, the well-defined orientation of 1d patterns, with defects perpendicular to the planar anchoring direction (*x*-axis in Fig. 3e), allows achieving a highly anisotropic ordering of the nanoparticles. When metallic or fluorescent nanoparticles are considered, the nanoparticle-liquid crystal composite shows highly anisotropic optical properties.

It has been shown that topological defects of the 1d patterns, expected to include dislocations, not only trap but also efficiently align nanorods [27, 43]. Indeed, the localization of nanorods within and parallel to the defect core maximizes the volume of disordered LC replaced by the nanorods and thus decreases the disorder energy of the core. The free energy per unit of length of a dislocation has been measured in free-standing 8CB smectic films to be around 0.5 k_BT/Å [87]. Therefore, one nanorod with a length of 20 nm trapped in the dislocation core decreases the LC disorder energy by around 115 k_BT, which significantly reduces the energy and stabilizes the defect. Once trapped in smectic dislocations, the nanorods may be stabilized with an orientation parallel to the defects and, therefore, parallel to each other in a well-aligned 1d array of defects [27, 43]. As a result, the emission of CdSe/CdS fluorescent nanorods trapped in 1d topological defects is efficiently polarized parallel to the defects (Fig. 9a-b) [43].

When the concentration of nanorods is larger than a few nanorods per μm^2, the nanorods form close-packed chains due to an enhanced nanoparticle diffusion parallel to the defects within the defect cores, leading to collisions between the confined nanoparticles [27]. As a result, highly anisotropic absorption of light is obtained using gold nanorods, such that plasmonic absorption can be controlled by varying the polarization of the incident light relative to the defect orientation (Fig. 9c) [27]. Nanorod chains are also promising for applications. A polarization-sensitive enhanced electromagnetic field can be created between two neighboring gold nanorods along the chains. The enhancement is expected to be particularly intense due to the small interparticle distance in the chains of the order of 1.7 nm [27]. This distance is controlled by the interdigitation between the ligands coating the nanoparticles.

Figure 9 – see end of the document

Combining spectrophotometry and Rutherford back-scattering (RBS) measurements in 8CB samples containing gold nanospheres, the surface density of nanospheres associated with chain formation can be evaluated for a given thickness and period of the 1d patterns. Based on the number of nanospheres that can be close-packed in one line defect to form one nanochain, it has been found that the maximum amount of nanospheres forming chains was close to the amount necessary to fully fill five 1d defects per hemicylinder. If only two dislocations are formed per hemicylinder, at the extremity of the two rotating grain boundaries, this result suggests that other line defects are present, namely both dislocations and disclinations, respectively at the basis and top of the curvature walls between neighboring hemicylinders. On the other hand, since we do not expect more than five line defects per hemicylinder, this result shows that the line defects can be almost entirely filled by nanoparticle chains without forming other types of aggregates. This also demonstrates that the cores of line defects are highly favorable sites for trapping gold nanospheres when the diameter of the nanoparticles does not exceed a few nanometers. As a result, long nanoparticle chains can be formed and effectively oriented in these line defects.

When the concentration of gold nanospheres was further increased, POM observations revealed that nanoparticles also formed one ribbon-like aggregate per hemicylinder (Fig. 10c). These aggregates most likely are nanoparticles confined within the central grain boundaries of the flattened hemicylinders (in green in Fig. 5). Indeed, GISAXS results for gold nanospheres with a diameter of 6 nm revealed a 2d hexagonal network parallel to the substrate (Fig. 10b), i.e., with the same orientation as the horizontal central grain boundaries [20]. Because these

grain boundaries have a large size of the order of 400 nm [49], the orientation of the hexagonal network is expected to vary randomly within the grain boundary. Instead, TSAXS and GISAXS showed that the ribbon-like hexagonal networks share a preferred orientation. Namely, the <10> direction, which is the dense direction of the of the 2d hexagonal network, is parallel to the hemicylinder axis. While the origin of the orientation of the nanoparticle chains confined in line defects is clear, it is less obvious why 2d nanoparticle networks should have any in-plane orientation within the central grain boundaries. Most likely, the ligands that coat nanoparticles (dodecanethiol for the gold nanospheres) interact with the 8CB molecules in such a way that the nanoparticles network couples to the smectic layers below the grain boundary. These smectic layers are perpendicular to the planar anchoring direction on the substrate (see Fig. 5), all parallel to each other and might guide the nanoparticle orientation. Therefore, we expect that the nature of the ligands affects the guiding efficiency of the 2d nanoparticle networks by the smectic matrix.

Once the line defects are filled by nanoparticle chains, the coexistence between nanoparticle chains and 2d hexagonal networks, respectively confined in line defects and horizontal grain boundaries, affects the optical properties of the composite. Chains of gold nanospheres are characterized by anisotropic light absorption despite the isotropic shape of the nanospheres. Figure 10a shows the light absorption of gold nanospheres chains (diameter 6 nm) perpendicular (in black) and parallel (in red) to the 1d patterns, i.e., perpendicular and parallel to the 1d defects. For parallel polarization, the absorption wavelength ($\lambda_{//}$) is larger than for perpendicular polarization ($\lambda_{\perp}$) due to the electromagnetic coupling between nanoparticles occurring along chains confined and oriented by the 1d defects. In contrast, the light absorption of 2d hexagonal networks is isotropic with $\lambda_{//} = \lambda_{\perp}$ as shown by the graph of Fig. 10d for large nanoparticle concentration. Fig. 10b shows how light absorption anisotropy varies when the nanoparticle concentration increases. Chains are obtained at low concentration, with $\lambda_{//} > \lambda_{\perp}$ (blue star dots). As the concentration increases (from left to right), the experimental data approach the line of unitary slope (violet dots). The optical absorbance of the composite combines those of nanoparticle chains and 2d hexagonal networks. The evolution of Fig. 10b is thus explained by the influence of the latter increasing with increasing nanoparticle concentration, the proportion of the hemicylinder central grain boundaries being filled by 2d hexagonal networks indeed increasing with nanoparticle concentration.

Figure 10 – see end of the document

Because topological defects are well oriented in thin smectic films under unidirectional hybrid anchoring conditions, they provide a useful template to create original nanoparticle organizations that are particularly difficult to achieve otherwise. Indeed, the enhanced diffusion of nanoparticles within line defects leads to small gaps and strong electromagnetic coupling between nanoparticles, producing highly anisotropic optical properties. Line defects effectively orient nanorods and nanoparticle chains. A priori, 2d hexagonal networks of gold nanospheres confined in the 2d grain boundary defects are also oriented along the defects, due to coupling with the smectic layers below the grain boundary. If extended to anisotropic nanoparticles, these 2d networks can lead to new kinds of assemblies with novel optical properties if the anisotropic nanoparticle themselves can be oriented in the grain boundaries. The presence of different kinds of topological defects in the same sample creates different kinds of coexisting nanoparticle assemblies, localized in different areas of the sample (either in line defects or in the central grain boundaries shown in Fig. 5b) that are close to each other. Rich perspectives are then opened based on the possible interaction both between nanoparticles within the assemblies or between the assemblies. In addition, thanks to the different nature of the defects, one of the defects is more favorable for nanoparticle trapping leading to the possibility of sequentially building the different kinds of nanoparticle assemblies.

3. 2. Manipulation of 1d patterns

It has recently been shown that both the localization and orientation of 1d patterns formed in air can be manipulated on a single substrate inducing unidirectional planar anchoring. 1d patterns of "nanogrooves" are formed in an open film when the substrate is patterned using microchannels that induce unidirectional planar anchoring [88]. Photopatterning of the substrate provides an efficient way to obtain many different large-scale patterns with precise localization on a single substrate [44]. This is promising for controlling the localization of topological defects. Moreover, new kinds of defects have been obtained at the boundaries between two 1d patterns of different orientations.

1d patterns can rotate on the substrate as a function of an external control parameter. Firstly, a 19° rotation was obtained by applying an electric field of the order of 1V/μm parallel to the substrate. The field, however, must be applied in the *N* phase to avoid the large energy barriers that hinder a change of topology in the smectic phase [44]. Secondly, 1d patterns can rotate as much as 12° near the N-S_A transition when 8CB is doped with a chiral dopant. The rotation angle depends on the temperature and has been ascribed to a surface electroclinic effect [89]. This effect might involve the perpendicular layers at the basis of the 1d patterns (see Fig. 5b), which rotate accordingly close to the N-S_A transition and drive the rotation of the whole hemicylinder above. Different rotation angles have been obtained for PI and PVA, possibly due to a different structure of the 1d patterns near the substrate.

4. Conclusions

In this review, we have outlined common structural features of 1d patterns created in S_A films either under unidirectional hybrid anchoring conditions or by applying an electric field. All patterns comprise cylindrical domains where smectic layers are folded confocally around a disclination line that is perpendicular to the planar anchoring direction and the applied electric field. The 1d pattern structure, however, varies and eventually transforms into 2d patterns as a function of the film thickness or electric field strength. For sufficiently thin S_A films close to the N-S_A phase transition temperature, an "intermediate" smectic phase appears, with undercooled *N* domains and partial penetration of the bend distortion. These domains most likely evolve into the topological defects observed at room temperature. Under unidirectional hybrid anchoring conditions, the topological defects have been identified using x-ray scattering experiments. The majority of defects have a 1d structure (line defects), in particular dislocations localized at the extremity of a rotating grain boundary that replaces the disclination line. Such replacement appears to be a general feature for all substrates considered. As the film thickness increases, the disclination transforms into a virtual disclination buried beneath the substrate inducing planar anchoring. On rubbed PVA substrates, a 2d defect was revealed in the form of a horizontal ribbon-like grain boundary joining smectic layers perpendicular to each other. The 1d patterns can be manipulated with electric fields applied in the *N* phase, whereas large energy barriers severely limit the topological changes that may be created by the applied field directly in S_A phase. An electric field perpendicular to the substrate reduces the effective thickness of the director distortion

and leads to a transition from 2d to 1d patterns, whereas electric fields applied parallel to the substrate produce a 19° in-plane rotation of the 1d pattern. The topological defects, being well oriented perpendicular to the unidirectional anchoring direction, are particularly efficient as orienting templates for confinement-induced nanoparticle organizations. Both nanospheres and nanorods can be trapped and oriented in the line defects, allowing to decrease the disorder energy of the defect core. The 2d defects unexpectedly lead to confinement-induced oriented hexagonal networks of nanospheres. A specific coupling between the nanoparticle ligands and the smectic layers below the grain boundaries is suggested to be at the origin of such orientation.

In perspective, more studies are necessary to elucidate the internal structure of the 1d patterns intimate structure, also for building new kinds of nanoparticle-LC composites and manipulating the nanoparticle optical properties. The location and temperature evolution of the undercooled *N* domains formed near the N-S_A transition temperature needs further investigation. It is also highly likely that a number of topological defects may be dispersed along the vertical curvature walls that join the hemicylinders within the 1d patterns. In such context, the use of the new x-ray microbeams now available at the 4^{th} generation synchrotron sources might be decisive. On the other hand, the demonstration of 2d networks of oriented nanoparticles is promising since they involve a large number of nanoparticles and lead to a large optical signal. The observation that close-packed nanoparticles form well-defined ordered networks also suggests the possible establishment of new kinds of collective optical features in these confinement-induced nanoparticle assemblies.

References

1. Friedel, G., Ann. Phys. (Paris), 1922. **18**: p. 273.
2. Lavrentovich, O.D. and V.M. Pergamenshchik, *Stripe Domain Phase of a Thin Nematic Film and the K13 Divergence Term.* Phys. Rev. Lett., 1994. **73**(7): p. 979-982.
3. Manyuhina, O.V. and M. Ben Amar, *Thin nematic films: Anchoring effects and stripe instability revisited.* Phys. Rev. A, 2013. **377**(13): p. 1003-1011.
4. Liang, H.L., et al., *Nematic-Smectic Transition under Confinement in Liquid Crystalline Colloidal Shells.* Phys. Rev. Lett., 2011. **106**(24): p. 247801.
5. Gooden, C., et al., *Simultaneous Magnetic-Deformation and Light-Scattering Study of Bend and Twist Elastic-Constant Divergence at the Nematic Smectic-a-Phase Transition.* Phys. Rev. Lett., 1985. **54**(10): p. 1035-1038.
6. Lonberg, F. and R.B. Meyer, *New ground-state for the splay-Freedericksz transition in a polymer nematic liquid-crystal.* Phys. Rev. Lett., 1985. **55**(7): p. 718-721.
7. Goscianski, M., L. Leger, and A. Mircea-Roussel, *Field induced transitions in smectic a phases.* J. Phys. Lett., 1975. **36**: p. 313-316.
8. Gryn, I., et al., *Controlling the self-assembly of periodic defect patterns in smectic liquid crystal films with electric fields.* Adv. Funct. Mater., 2015. **25**(1): p. 142-149.
9. Parodi, O., *A possible magnetic transition in smectics-A.* Solid State Comm., 1972. **11**: p. 1503-1507.
10. Zola, R.S., et al., *Dynamic Control of Light Direction Enabled by Stimuli-Responsive Liquid Crystal Gratings.* Advanced Materials, 2019. **31**(7).
11. Kim, Y.H., et al., *Optically Selective Microlens Photomasks Using Self-Assembled Smectic Liquid Crystal Defect Arrays.* Adv. Mater., 2010. **22**(22): p. 2416.
12. Serra, F., et al., *Curvature-Driven, One-Step Assembly of Reconfigurable Smectic Liquid Crystal "Compound Eye" Lenses.* Adv. Opt. Mater., 2015. **3**(9): p. 1287-1292.
13. Son, B., et al., *Optical vortex arrays from smectic liquid crystals.* Opt. Express, 2014. **22**(4): p. 4699-4704.
14. Oswald, P. and P. Pieranski, *Smectic and columnar liquid crystals*, ed. T. Francis. 2006: Taylor & Francis.
15. De Gennes, P.G., *An analogy between superconductors and smectics A.* Solid State Comm., 1972. **10**: p. 753-756.
16. Peddireddy, K., et al., *Lasing and waveguiding in smectic A liquid crystal optical fibers.* Optics Express, 2013. **21**(25): p. 30233-30242.
17. Peddireddy, K., et al., *Self-shaping liquid crystal droplets by balancing bulk elasticity and interfacial tension.* Proceedings of the National Academy of Sciences, 2021. **118**(14): p. e2011174118.
18. De Gennes, P.G. and J. Prost, *The Physics of Liquid Crystals (2nd Ed.)*. 1993, Oxford, UK: Oxford University Press.
19. Choi, M.C., et al., *Ordered patterns of liquid crystal toroidal defects by microchannel confinement.* Proc. Nat. Acad. Sci. U.S.A., 2004. **101**(50): p. 17340-17344.
20. Do, S.-P.h., et al., *From Chains to Monolayers: Nanoparticle Assembly Driven by Smectic Topological Defects.* Nano Letters, 2020. **20**(3): p. 1598-1606.
21. Yoon, D.K., et al., *Internal structure visualization and lithographic use of periodic toroidal holes in liquid crystals.* Nat. Mater., 2007. **6**(11): p. 866-870.
22. Coursault, D., et al., *Linear self-assembly of nanoparticles within liquid crystal defect arrays.* Adv. Mater., 2012. **24**(11): p. 1461-1465.
23. Milette, J., et al., *Reversible long-range patterning of gold nanoparticles by smectic liquid crystals.* Soft Matter, 2012. **8**(24): p. 6593-6598.
24. Coursault, D., et al., *Tailoring anisotropic interactions between soft nanospheres using dense arrays of smectic liquid crystal edge dislocations.* ACS Nano, 2015. **9**(12): p. 11678-11689.
25. Honglawan, A., et al., *Synergistic assembly of nanoparticles in smectic liquid crystals.* Soft Matter, 2015. **11**(37): p. 7367-7375.
26. Gryn, I., et al., *Electric-field-controlled alignment of rod-shaped fluorescent nanocrystals in smectic liquid crystal defect arrays.* Adv. Funct. Mater., 2016. **26**(39): p. 7122-7131.
27. Rozic, B., et al., *Oriented Gold Nanorods and Gold Nanorod Chains within Smectic Liquid Crystal Topological Defects.* ACS Nano, 2017. **11**(7): p. 6728-6738.
28. Kim, Y.H., et al., *Fabrication of a Superhydrophobic Surface from a Smectic Liquid-Crystal Defect Array.* Adv. Funct. Mater., 2009. **19**(18): p. 3008-3013.
29. Kim, Y.H., et al., *Smectic Liquid Crystal Defects for Self-Assembling of Building Blocks and Their Lithographic Applications.* Adv. Funct. Mater., 2011. **21**(4): p. 610-627.
30. Designolle, V., et al., *AFM Study of Defect-Induced Depressions of the Smectic-A/Air Interface.* Langmuir, 2006. **22**(1): p. 363-368.
31. Gim, M.J., D.A. Beller, and D.K. Yoon, *Morphogenesis of liquid crystal topological defects during the nematic-smectic A phase transition.* Nat. Comm., 2017. **8**: p. 1-9.
32. Cladis, P.E. and S. Torza, *Growth of a smectic A from a bent nematic phase and the smectic light valve.* J. Appl. Phys., 1975. **46**: p. 584-599.

33. Ruan, L.Z., J.R. Sambles, and I.W. Stewart, *Self-organized periodic photonic structure in a nonchiral liquid crystal.* Phys. Rev. Lett., 2003. **91**(3): p. 033901.
34. Pishnyak, O.P., Y.A. Nastishin, and O.D. Lavrentovich, *Comment on ``Self-Organized Periodic Photonic Structure in a Nonchiral Liquid Crystal".* Physical Review Letters, 2004. **93**(10): p. 109401.
35. Zappone, B., et al., *Analogy between periodic patterns in thin smectic liquid crystal films and the intermediate state of superconductors.* Proceedings of the National Academy of Sciences, 2020. **117**(30): p. 17643-17649.
36. Oswald, P. and J. Colombier, *On the measurement of the bend elastic constant in nematic liquid crystals close to the nematic-to-SmA and the nematic-to-NTB phase transitions.* Liquid Crystals, 2021: p. 1-25.
37. Zappone, B., et al., *Periodic lattices of frustrated focal conic defect domains in smectic liquid crystal films.* Soft Matter, 2012. **8**(16): p. 4318.
38. Liang, H.L., et al., *Towards tunable defect arrangements in smectic liquid crystal shells utilizing the nematic-smectic transition in hybrid-aligned geometries.* Soft Matter, 2012. **8**(20): p. 5443-5450.
39. Allet, C., M. Kleman, and P. Vidal, *Striped patterns in a thin droplet of a smectic C phase.* J. Phys. France II, 1978. **39**: p. 181-188.
40. Michel, J.P., et al., *Optical gratings formed in thin smectic films frustrated on a single crystalline substrate.* Phys. Rev. E, 2004. **70**(1): p. 011709.
41. Michel, J.-P., et al., *Structure of smectic defect cores: X-ray study of 8CB liquid crystal ultrathin films.* Phys. Rev. Lett., 2006. **96**(2): p. 027803.
42. Lacaze, E., et al., *Planar anchoring and surface melting in the smectic-A phase.* Physical Review E, 2007. **76**(4): p. 041702.
43. Pelliser, L., et al., *Alignment of rod-shaped single-photon emitters driven by line defects in liquid crystals.* Adv. Funct. Mater., 2015. **25**(11): p. 1719-1726.
44. Wu, S.B., et al., *Smectic Defect Engineering Enabled by Programmable Photoalignment.* Advanced Optical Materials, 2020. **8**(17).
45. Fournier, J.B., I. Dozov, and G. Durand, *Surface frustration and texture instability in smectic-A liquid-crystals.* Phys. Rev. A, 1990. **41**(4): p. 2252-2255.
46. Blanc, C. and M. Kleman, *Curvature walls and focal conic domains in a lyotropic lamellar phase.* Eur. Phys. J. B, 1999. **10**(1): p. 53-60.
47. Zappone, B. and E. Lacaze, *Surface-frustrated periodic textures of smectic-A liquid crystals on crystalline surfaces.* Phys. Rev. E, 2008. **78**(6): p. 061704.
48. Zappone, B., et al., *Self-ordered arrays of linear defects and virtual singularities in thin smectic-A films.* Soft Matter, 2011. **7**(3): p. 1161-1167.
49. Coursault, D., et al., *Self-organized arrays of dislocations in thin smectic liquid crystal films.* Soft Matter, 2016. **12**(3): p. 678-88.
50. Nemitz, I.R., et al., *Observations of a streak texture in the hybrid-aligned smectic-C phase.* Soft Matter, 2018. **14**(3): p. 460-469.
51. Xia, J., et al., *Structural Landscapes in Geometrically Frustrated Smectics.* Physical Review Letters, 2021. **126**(17): p. 177801.
52. Kléman, M., *Points, lines and and walls in liquid crystals, magnetic systems and various ordered systems*. 1983, New York: Wiley.
53. Lacaze, E., et al., *Ordered interfaces for dual easy axes in liquid crystals.* Soft Matter, 2011. **7**(3): p. 1078-1083.
54. Yethiraj, A., *Recent experimental developments at the nematic to smectic-A liquid crystal phase transition*, in *Thermotropic liquid crystals: Recent advances*, A. Ramamoorthy, Editor. 2007, Springer
55. Pevnyi, M.Y., J.V. Selinger, and T.J. Sluckin, *Modeling smectic layers in confined geometries: Order parameter and defects.* Physical Review E, 2014. **90**(3): p. 032507.
56. Poole, C.P., et al., *Superconductivity, chap. 11*. 2007, London, UK: Academic Press.
57. Prozorov, R., *Equilibrium topology of the intermediate state in type-I superconductors of different shapes.* Phys. Rev. Lett., 2007. **98**(25): p. 257001.
58. Prozorov, R., et al., *Suprafroth in type-I superconductors.* Nat. Phys., 2008. **4**(4): p. 327-332.
59. Renn, R. and T.C. Lubensky, *Abrikosov dislocation lattice in a model of the cholesteric - to - smectic-A transition.* Phys. Rev. A, 1988. **38**: p. 2132-2147.
60. Nguyen, H.T., et al., J. Phys. France II, 1992. **2**: p. 1889-1906.
61. Nastishin, Y.A., et al., *Identification of a TGBA liquid crystal phase via its defects.* European Physical Journal E, 2001. **5**(3): p. 353-357.
62. Asnacios, S., et al., *Rheological properties of chiral liquid crystals possessing a cholesteric-smectic A transition.* Liquid Crystals, 2004. **31**(4): p. 593-599.
63. Ruan, L.Z., M.A. Osipov, and J.R. Sambles, *Coexisting nematic and smectic-A phases in a twisted liquid-crystal cell.* Phys. Rev. Lett., 2001. **86**(20): p. 4548-4551.
64. Dozov, I. and G. Durand, *Quantized grain boundaries in bent smectic-A liquid crystals.* Eur. Phys. Lett., 1994. **28**(1): p. 25-30.
65. Wang, R.T., et al., *Bend-induced melting of the smectic-A phase: Analogy to a type-I superconductor.* Phys. Rev. Lett., 2006. **97**(16): p. 167802.
66. Nobili, M. and G. Durand, *Disorientation-Induced Disordering at a Nematic-Liquid-Crystal Solid Interface.* Physical Review A, 1992. **46**(10): p. R6174-R6177.

67. Wittebrood, M.M., et al., *Confinement effects on the collective excitations in thin nematic films.* Physical Review Letters, 1998. **80**(6): p. 1232-1235.
68. Ma, L.-L., et al., *Smectic Layer Origami via Preprogrammed Photoalignment.* Advanced Materials, 2017. **29**(15): p. 1606671.
69. Rapini, A., *Instabilités magnétiques d'un smectique C.* Journal de Physique Colloques, 1972. **33**: p. 237-247.
70. Jones, C., *Bistable liquid crystal displays*, in *Handbook of visual display technology*, J. Chen, W. Cranton, and M. Fihn, Editors. 2012, Springer: Berlin.
71. Lavrentovich, O.D., M. Kléman, and V.M. Pergamenshchik, *Nucleation of focal conic domains in smectic A liquid crystals.* Journal de Physique II 1994. **4**: p. 377-404.
72. Li, Z. and O.D. Lavrentovich, *Surface Anchoring and Growth Pattern of the Field-Driven First-Order Transition in a Smectic-A Liquid Crystal.* Physical Review Letters, 1994. **73**(2): p. 280-283.
73. Contreras, A., et al., *The onset of layer undulations in smectic A liquid crystals due to a strong magnetic field.* Nonlinearity, 2016. **29**(8): p. 2474-2496.
74. Hinov, H.P., *Formation of a smectic A phase from a strongly deformed planar nematic liquid crystal CBOOA.* Journal de Physique, 1981. **42**(2): p. 307-315.
75. Hinov, H.P. and V.G.K.M. Pisipati, *Influence of the smectic A-nematic transitional order on the formation of the smectic phases of 4-n-hexyloxybenzylidene-4'-n-butylaniline and 4-n-butyloxybenzylidene-4'-n-octylaniline from an electrically deformed nematic phase.* Mol. Cryst. Liq. Cryst., 1990. **8**(2): p. 193-209.
76. Hareng, M., S.L. Berre, and L. Thirant, *Electric field effects on biphenyl smectic A liquid crystals.* Applied Physics Letters, 1974. **25**(12): p. 683-685.
77. Jákli, A. and A. Saupe, *Electro-Optic Effects in Smectic a Phase.* Molecular Crystals and Liquid Crystals Science and Technology. Section A. Molecular Crystals and Liquid Crystals, 1992. **222**(1): p. 101-109.
78. Findon, A., H. Gleeson, and J. Lydon, *Realignment of a smectic-A phase with applied electric field.* Physical Review E, 2000. **62**(4): p. 5137-5142.
79. Boniello, G., et al., *Making Smectic Defect Patterns Electrically Reversible and Dynamically Tunable Using In Situ Polymer-Templated Nematic Liquid Crystals.* Macromolecular Rapid Communications, 2021. **42**(11): p. 2100087.
80. Senyuk, B., et al., *Shape-Dependent Oriented Trapping and Scaffolding of Plasmonic Nanoparticles by Topological Defects for Self-Assembly of Colloidal Dimers in Liquid Crystals.* Nano Letters, 2012. **12**(2): p. 955-963.
81. Yoshida, H., et al., *Nanoparticle-Stabilized Cholesteric Blue Phases.* Applied Physics Express, 2009. **2**(12): p. 121501.
82. Karatairi, E., et al., *Nanoparticle-induced widening of the temperature range of liquid-crystalline blue phases.* Physical Review E, 2010. **81**(4): p. 041703.
83. Rožič, B., et al., *Theoretical and experimental study of the nanoparticle-driven blue phase stabilisation.* The European Physical Journal E, 2011. **34**(2): p. 17.
84. Cordoyiannis, G., et al., *Different modulated structures of topological defects stabilized by adaptive targeting nanoparticles.* Soft Matter, 2013. **9**(15): p. 3956-3964.
85. Evans, J.S., et al., *Optical generation, templating, and polymerization of three-dimensional arrays of liquid-crystal defects decorated by plasmonic nanoparticles.* Physical Review E, 2013. **87**(3): p. 032503.
86. Gharbi, M.A., et al., *Reversible Nanoparticle Cubic Lattices in Blue Phase Liquid Crystals.* ACS Nano, 2016. **10**(3): p. 3410-3415.
87. Geminard, J.C., C. Laroche, and P. Oswald, *Edge dislocation in a vertical smectic-A film: Line tension versus film thickness and Burgers vector.* Physical Review E, 1998. **58**(5): p. 5923-5925.
88. Kim, D.S., et al., *Fast Fabrication of Sub-200-nm Nanogrooves Using Liquid Crystal Material.* Acs Applied Materials & Interfaces, 2016. **8**(18): p. 11851-11856.
89. Nemitz, I.R., et al., *Chiral oily streaks in a smectic-A liquid crystal.* Soft Matter, 2016. **12**(31): p. 6662-6668.
90. Guo, W. and C. Bahr, *Influence of anchoring strength on focal conic domains in smectic films.* Physical Review E, 2009. **79**(1): p. 011707.

FIGURE 1

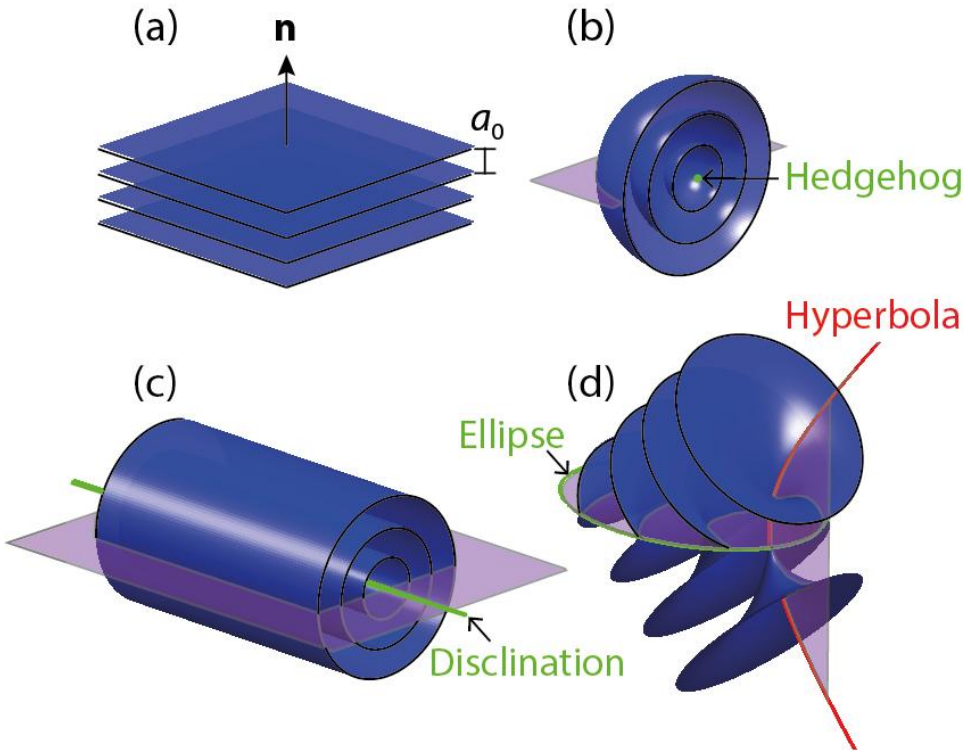

Figure 1. Smectic layers (blue) stacked in confocal structures with uniform layer spacing a_0 and director **n** normal to the layers. The layer's centers of curvature (red and green) are topological defects of the director field. On the purple planes, **n** is parallel to the plane. The director on the planes shown in pink makes a **(a)** Smectic ground state, **(b)** Concentric spheres. **(c)** Concentric cylinders (roll). **(d)** Focal conic domain (FCD) with centers of curvature lying on a conjugated pair of focal conics (ellipse and hyperbola).

FIGURE 2

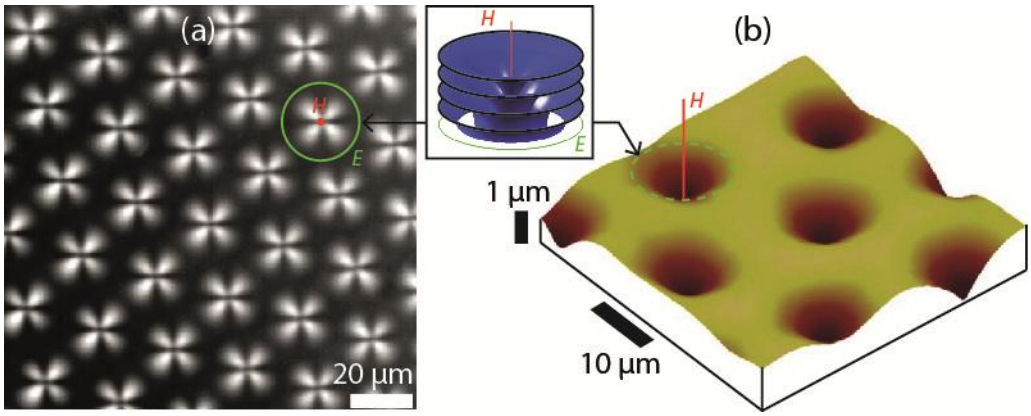

Figure 2. (a) POM image of a honeycomb lattice of toroidal FCDs obtained in a smectic film with degenerate hybrid conditions. *H* is a straight line perpendicular to the surfaces and *E* is a circle lying flat on the surface that induces the degenerate planar anchoring. Reproduced from ref. [46] with permission from Springer Nature publishing group. **(b)** AFM topographic 3d image of the free interface between air and an 8CB film, showing that each FCD produces a depression at the interface of shallow depth, of the order of ….. Adapted from ref. [90] with permission from the American Physical Society.

FIGURE 3

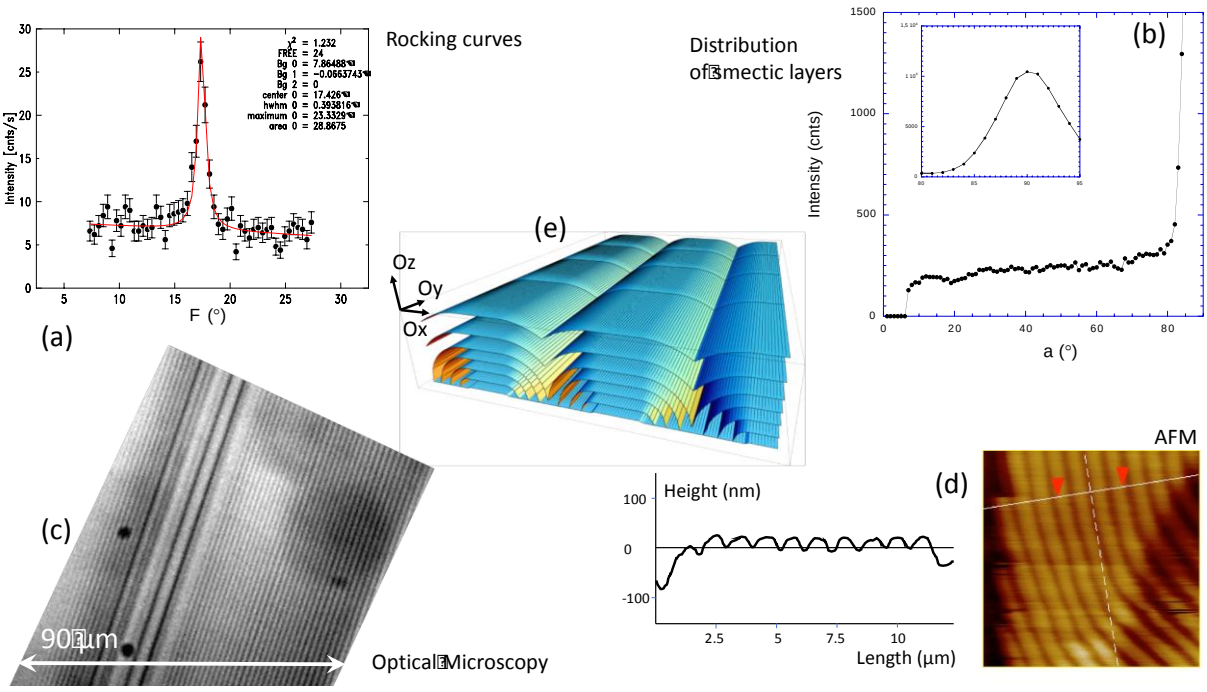

Figure 3. Analysis of the internal structure of 8CB films of thickness varying between $h \approx$ 450 and h ≈ 130 nm deposited on molybdenite in air, adapted from ref. [40] with permission from the American Physical Society. **(a)** x-ray scattering intensity as a function of the orientation Φ of the wave-vector transfer in the substrate plane ($h \approx$ 450 nm). **(b)** x-ray scattering intensity ($h \approx$ 450 nm) measured by tilting the wave-vector transfer away from the substrate. The tilt angles α = 7° and α = 80° corresponded to an almost parallel and almost normal orientation, respectively. No intensity was detected between α = 0° and α = 7° due to the threshold angle below which no x-ray intensity could penetrate the 8CB film **(c)** POM image between cross polarizers of the 8CB film revealing straight and parallel stripes ($h \approx$ 200 nm). The large stripe in the middle corresponds to a locally different structure. **(d)** AFM topographic 2d image of the free surface of the 8CB film ($h \approx$ 130 nm) revealing a straight and parallel surface undulation with a depth of the order of 10 nm, shown by the profile (left side) performed for the line displayed on the AFM picture (right side). **(d)** Model of the 1d patterns where *x*-axis corresponds to the anchoring direction and *xy* is the substrate plane.

FIGURE 4

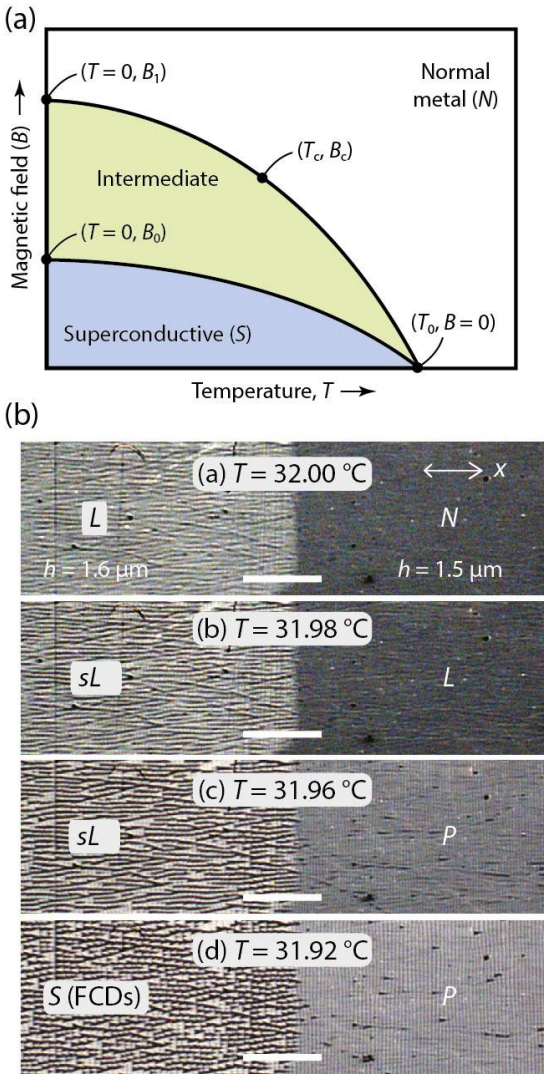

Figure 4 (a). Schematic phase diagram of a type-I metal showing an intermediate state (*P*) between the normal (*N*) and superconductive (*S*) state. The magnetic field (*B*) is completely expelled from the latter state, whereas it penetrates in the intermediate state via finite-sized domains of undercooled *N* domains. T_c and B_c are the critical temperature and field of the transition from the normal state. In a LC, *N*, *S*, and *P* are the nematic, smectic, and intermediate phase, respectively, whereas *B* is the magnitude of the bend distortion. **(b)** Textures observed in across a step of thickness upon cooling a 8CB film with large ($h > 1.5$ μm) and small ($h \leq 1.5$ μm) thickness. *x* is the planar anchoring direction. *L* is an undulation of the *N* phase that evolves into the FCDs of the *S* phase. Adapted from ref. [35] with permission from the Proceedings of the National Academy of Sciences of the U.S.A.

FIGURE 5

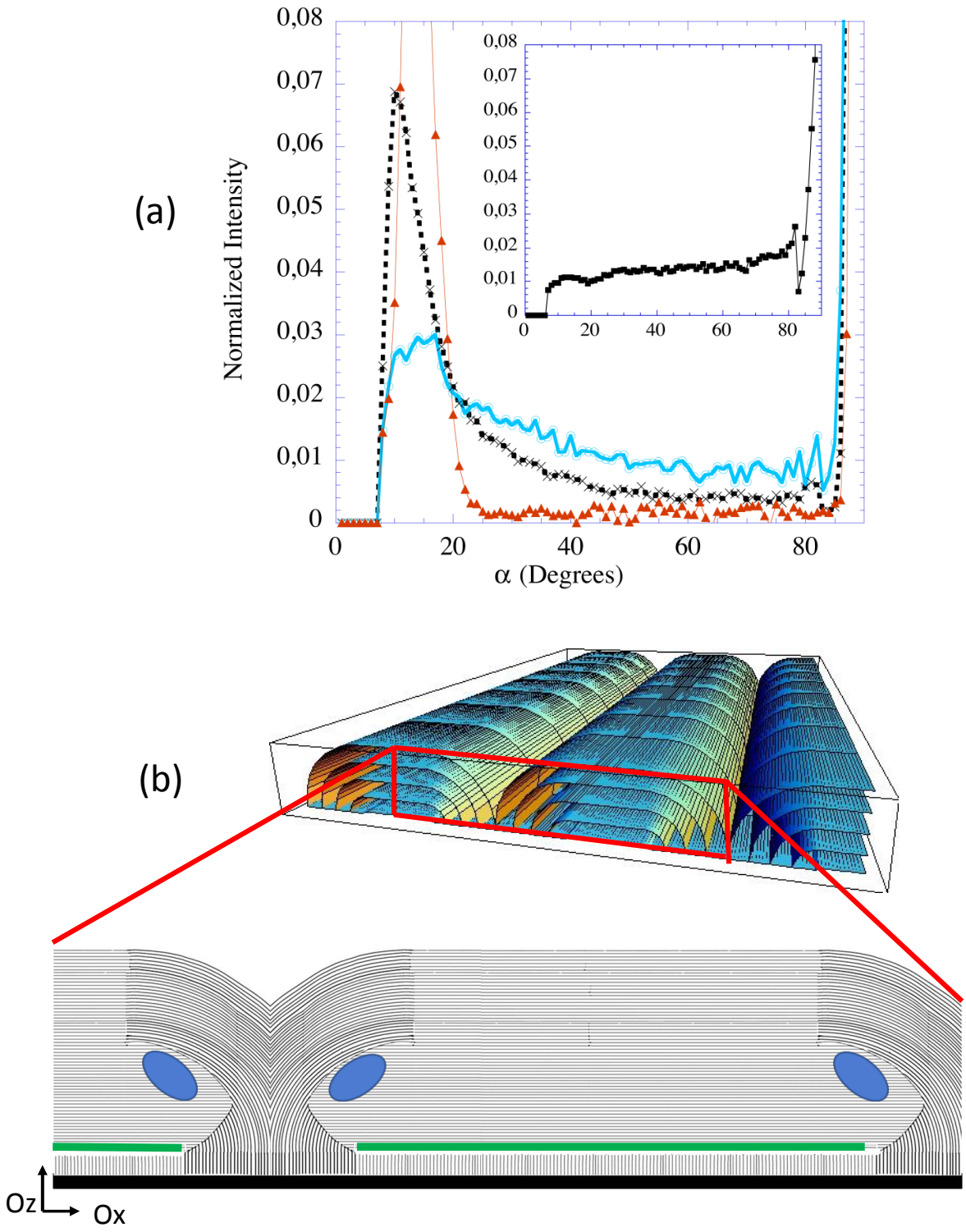

Figure 5. (a) x-ray scattering intensity as a function of the wave-vector transfer tilt angle α for 8CB films deposited on molybdenite in air with various thicknesses: $h \approx 450$ nm (insert) to $h \approx 200$ nm (blue open circles), $h \approx 150$ nm (black crosses), $h \approx 70$ nm (red triangles), adapted

from ref. [41] with permission from the American Physical Society. **(b)** Model of the 1d patterns (in perspective: adapted from ref. [40] with permission from the American Physical Society) seen in side-view on PVA, (*xz* plane) where the topological defects are shown in blue for the dislocations at the upper part of the rotating grain boundary and in green for the central grain boundary.

FIGURE 6

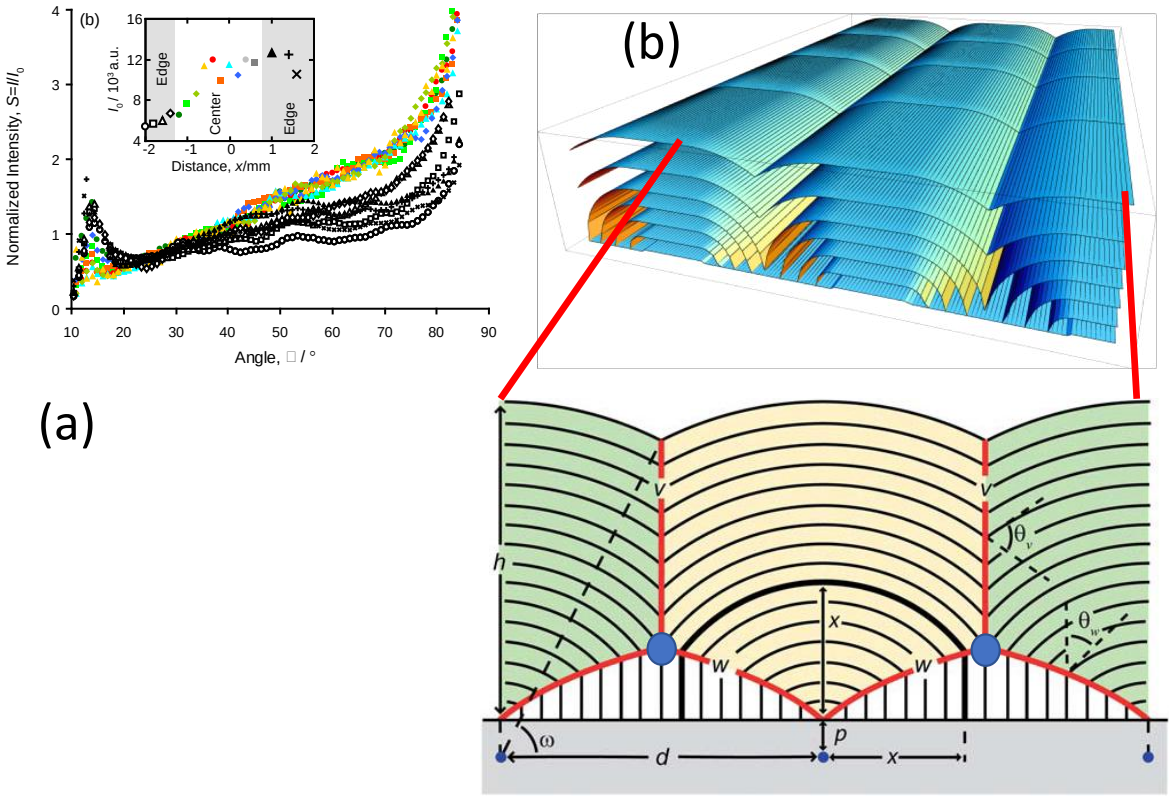

Figure 6. Structural study of an open 8CB film of thickness around 1µm on mica, adapted from ref. [48] with permission from the Royal Society of Chemistry. **(a)** x-ray scattering intensity as a function of wave-vector transfer tilt angle α. The measurements were done along an 8CB droplet spreading on the mica substrate for different thicknesses defined by the position of the x-ray beam relative to the droplet border. The integrated intensity is displayed in the inset as a function of the position relative to the droplet border. **(b)** Model of 1d pattern extracted from the x-ray data.

FIGURE 7

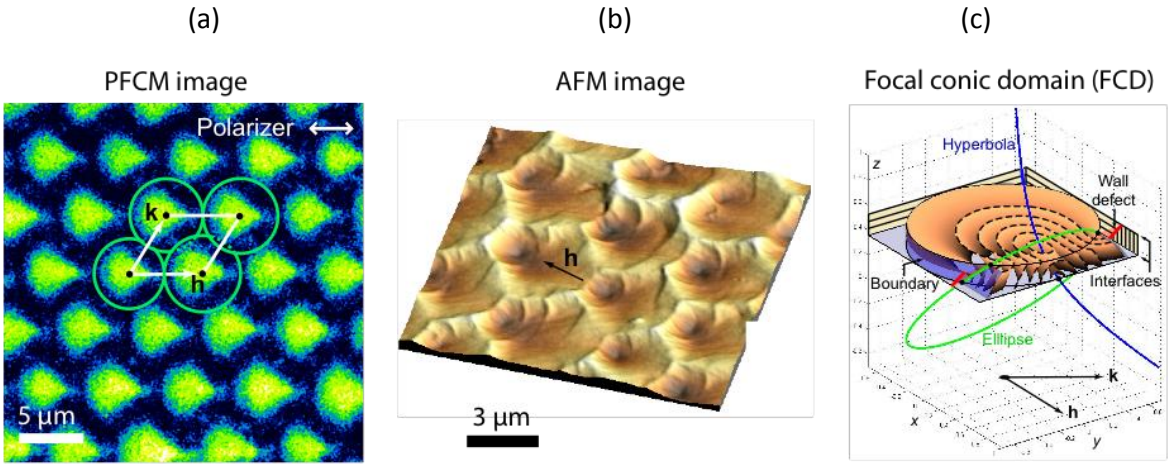

Figure 7. Structural study of an open 8CB film of thickness around 1.5 µm deposited on rubbed PI, adapted from ref. [37] with permission from the Royal Society of Chemistry. **(a)** FCPEM image of a 2d pattern of non-toroidal FCDs. **(b)** AFM topographic 3d image of the free surface. **(c)** Model of the 2d pattern model**.**

FIGURE 8

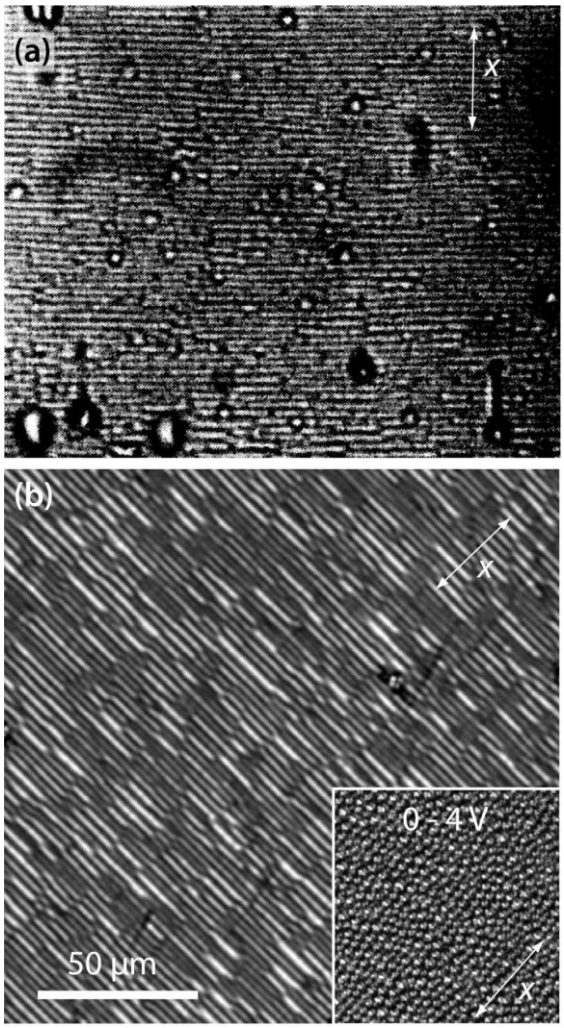

Figure 8. **(a)** 1d pattern obtained by applying an electric field normal to an 8OCB film with planar anchoring conditions. The field was applied in the S_A phase. Adapted from ref. [7] with permission from EDP Sciences. **(b)** 1d pattern induced by an electric field in an 8CB film with thickness h = 7.1 μm and hybrid planar-homeotropic anchoring conditions. The sample was cooled from the N to the S_A phase under a constant voltage V = 5 V. The inset shows the FCD texture obtained for lower voltages in the same region. Adpated from ref. [8] with permission from Wiley- VCH Verlag GmbH & Co. KGaA

FIGURE 9

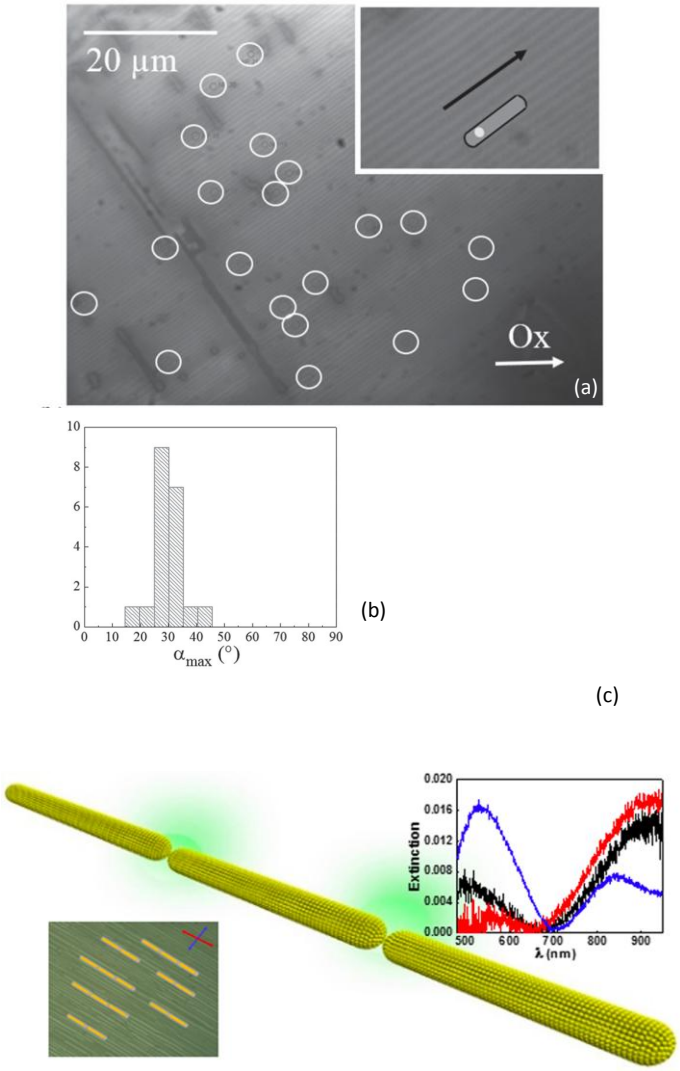

Figure 9. **(a)** 1d patterns of 8CB on rubbed PVA including fluorescent CdSe/CdS nanorods, whose localization is indicated by open circles (the insert indicates the nanorod orientation relative to the 1d pattern orientation). **(b)** Histogram of the polarization of the emitted light from the nanorods shown by the circles in (a). The angle α indicates the orientation of the analyzer, with α = 30° corresponding to a polarization parallel to the 1d patterns. Adapted from ref. [43] with permission from Wiley Online Library. **(c)** Extinction as a function of light wavelength of a composite 8CB/gold nanorods on rubbed PVA (in black, not polarized light, in blue and red, polarization respectively perpendicular and parallel to the 1d patterns

shown on the left, with the corresponding small chains schematized), adapted from ref. [27] with permission from the American Chemical Society.

FIGURE 10

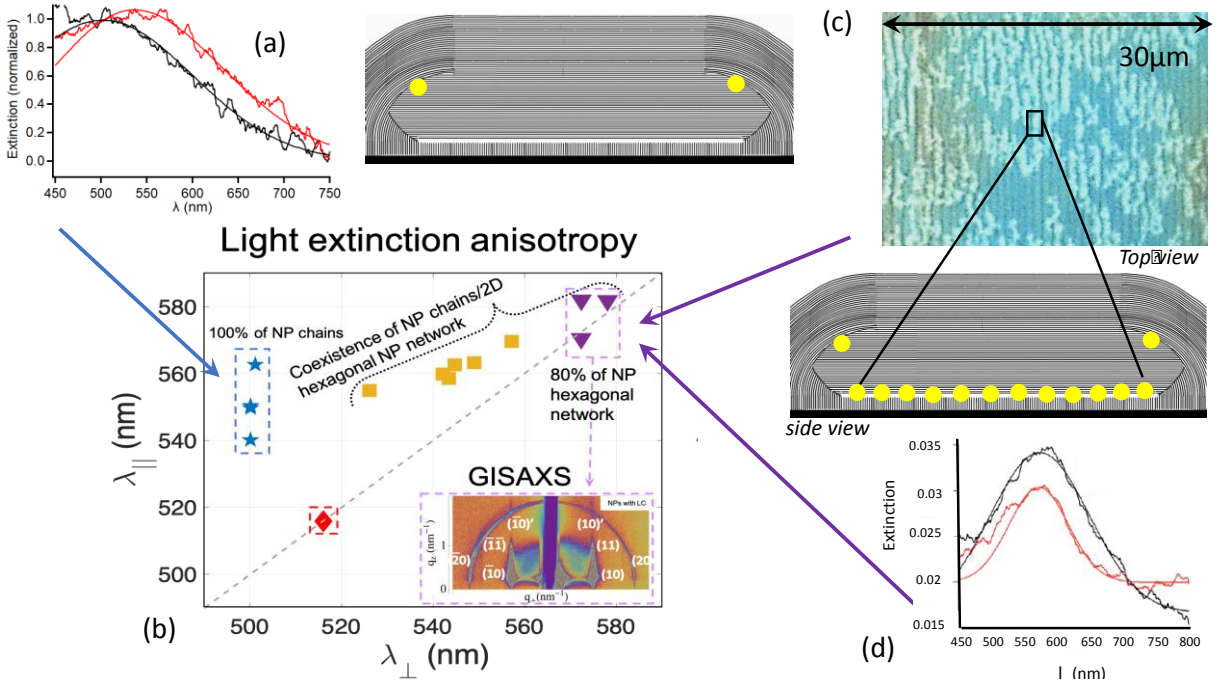

Figure 10. **(a)** Light extinction as a function of the wavelength λ for a low concentration of gold nanospheres (diameter 6 nm) dispersed in 8CB thin films on rubbed PVA. Black and red curves correspond to an incident beam polarized perpendicular and parallel to the 1d pattern, respectively. A side-view schematic of chain formation in a flattened hemicylinder is shown on the right. **(b)** Phase diagram for the coexistence of nanoparticle chains and 2d hexagonal networks as a function of the extinction values $\lambda_\perp$ (absorption wavelength for an incident beam polarized perpendicular to the 1d pattern) and $\lambda_\parallel$ (absorption wavelength for an incident beam polarized parallel to the 1d pattern), obtained for different samples and different sample regions. Blue stars, red diamonds, and purple triangles correspond respectively to nanoparticle chains, isolated nanoparticles in solution, and structures formed with the highest nanoparticle concentration, for which GISAXS results are also shown (displaying the various rods associated with a 2d hexagonal network). The dotted line with unit slope indicates isotropic optical properties ($\lambda_\perp = \lambda_\parallel$). **(c)** POM image of an 8CB film with a dense array of nanoparticle ribbons located within the 8CB hemicylinders which are seen in top view (one portion of a single ribbon is surrounded by a black rectangle). A side-view schematic of nanoparticle confinement in the central grain boundary of a flattened hemicylinder is shown below. **(d)** Light extinction as a function of the wavelength λ for a large concentration of gold

nanoparticles (Black and red curves correspond to an incident beam polarized perpendicular and parallel to the 1d pattern, respectively).